









# Seasonal Effects of the Changing Photon Scattering Rates on Mercury's Exospheric Structure

Matthew H. Burger<sup>1</sup> , Rosemary M. Killen<sup>2</sup> , Ronald J. Vervack, Jr.<sup>3</sup> , Orenthal J. Tucker<sup>4</sup> , Liam S. Morrissey<sup>5</sup> , and Daniel W. Savin<sup>6</sup> 

<sup>1</sup> Space Telescope Science Institute, 3700 San Martin Drive, Baltimore, MD 21218, USA; [mburger@stsci.edu](mailto:mburger@stsci.edu)

<sup>2</sup> NASA Goddard Space Flight Center, Planetary Magnetospheres Laboratory, Code 695, Greenbelt, MD 20771, USA

<sup>3</sup> Johns Hopkins Applied Physics Laboratory, 11100 Johns Hopkins Road, Laurel, MD 20723, USA

<sup>4</sup> Hampton University, Atmospheric and Planetary Sciences, 154 William R. Harvey Way, Hampton, VA 23668, USA

<sup>5</sup> Faculty of Engineering and Applied Science, Memorial University, St. Johns, NL A1B 2W4, Canada

<sup>6</sup> Columbia University, Columbia Astrophysics Laboratory, MC5247, 538 West 120th Street, New York, NY 10027, USA

Received 2025 April 22; revised 2025 September 30; accepted 2025 October 7; published 2025 November 14

## Abstract

Emission in Mercury's exosphere observed from the ground and by spacecraft is produced by resonant scattering of sunlight. The process of resonant scattering changes the structure of the exosphere owing to the transfer of momentum between the incident photons and the scattering atoms, resulting in a net antisunward-directed force known as radiation pressure. The photon scattering rate (the so-called  $g$ -value) and the magnitude of radiation pressure depend strongly on both Mercury's distance from the Sun and the radial velocities of the scattering atoms relative to the Sun. We discuss four effects of the changing  $g$ -value over a Mercury year that require a model capable of tracking the positions and speeds of exospheric constituents in order to properly interpret emission data: (1) variations in the escape flux of atoms, (2) variations in the ratio of atoms that escape Mercury in neutral versus ionized form, (3) difficulties in determining where material was ejected from the surface based on the locations of the emitting atoms in the exosphere, and (4) systematic uncertainties in interpreting the column density of emitting gas using a constant  $g$ -value versus a variable  $g$ -value that takes into account the radial motion of the atoms relative to the Sun.

*Unified Astronomy Thesaurus concepts:* [Mercury \(planet\) \(1024\)](#); [Exosphere \(499\)](#); [Astronomy data modeling \(1859\)](#); [Planetary atmospheres \(1244\)](#); [Solar-planetary interactions \(1472\)](#)

## 1. Introduction

Surface-bounded exospheres, atmospheres that are collisionless down to a planetary surface, are the most common type of atmosphere in the solar system and may be common in exoplanetary systems, as suggested by exoplanets thought to lack dense atmospheres such as LHS 3844b (L. Kreidberg et al. 2019) and Trappist 1b (T. P. Greene et al. 2023). The two most well-studied surface-bounded exospheres in the solar system are those of Mercury and the Moon (F. Leblanc et al. 2022; P. Wurz et al. 2022; A. Milillo et al. 2023). These tenuous atmospheres are in a constant state of creation and destruction. Material is actively ejected from the surface and removed from the exosphere by multiple processes (see R. M. Killen et al. 2018, and references therein). Source processes include photon-stimulated desorption (PSD), the process by which solar ultraviolet (UV) photons eject atoms from the top-most layer of grains in the regolith; micrometeoroid impact vaporization (MIV); and ion sputtering, where energetic solar wind ions bombard the surface, leading to the ejection of atoms from the regolith. There may also be a thermally desorbed component for some species (P. Lierle et al. 2022). Neutral atoms are removed from the exosphere by photoionization from solar UV radiation, collisions with the surface, or gravitational escape. Photo-ions are either picked up by the solar wind and removed from the Mercury system or trapped in the exo-ionosphere, where they can return to the surface.

Mercury's exosphere has been observed from the ground and by spacecraft (see W. E. McClintock et al. 2018, and references therein). Hydrogen and helium were first detected during the Mariner 10 flybys of Mercury (A. L. Broadfoot et al. 1976). Ground-based observations over the next several decades revealed sodium (A. Potter & T. Morgan 1985), potassium (A. E. Potter & T. H. Morgan 1986), and calcium (T. A. Bida et al. 2000), with tentative detections of aluminum and iron (T. A. Bida & R. M. Killen 2017). The UltraViolet and Visible Spectrometer (UVVS) channel of the Mercury Atmospheric and Surface Composition Spectrometer (W. E. McClintock & M. R. Lankton 2007) on the Mercury Surface, Space ENvironment, GEOchemistry, and Ranging (MESSENGER) spacecraft (S. C. Solomon & B. J. Anderson 2018) confirmed the presence of aluminum and added magnesium and manganese to the roster of known atomic species in the exosphere (W. E. McClintock et al. 2009; R. J. Vervack et al. 2016). Over the course of the four year MESSENGER mission, UVVS made near-daily observations of Na, Mg, and Ca (W. E. McClintock et al. 2018). Oxygen, expected to be abundant in the exosphere due to its high abundance in the regolith ( $\sim 40\%$  by mass; T. J. McCoy et al. 2018), was not seen by UVVS (R. J. Vervack et al. 2016), despite A. L. Broadfoot et al. (1976) having reported a possible detection by Mariner 10 (however, a reassessment of this data revised this to an upper limit; A. L. Broadfoot 2025, private communication) and the detection of oxygen-group ions (ions with mass to charge ratio equal to 16–20, such as  $O^+$ ,  $OH^+$ , and  $H_2O^+$ ) by the MESSENGER Fast Ion Plasma Spectrometer (H. Korth et al. 2018).

In this paper, we explore how the structure and loss rates from Mercury’s exosphere change due to variations in the solar radiation field caused by Mercury’s eccentric orbit. The importance of radiation pressure on the motions of Na atoms ejected from Mercury’s surface and the formation of a comet-like tail directed away from the Sun was first recognized by W. H. Ip (1986) and W. H. Smyth (1986). In particular, they pointed out that the escape flux has a strong dependence on Mercury’s true anomaly angle (TAA). We expand on those results by examining the importance of tracking velocity variations along a particle trajectory, especially the component along the Sun–Mercury axis, in order to understand variations in photon emission rates and radiation acceleration. In Section 2, we show for exospheric neutral Na and Ca how variations in the photon scattering rate and the corresponding variations in radiation pressure experienced by these atoms complicate the interpretation of observations and make it difficult to determine the surface distribution of the corresponding exospheric sources. In Section 3, we demonstrate that the radial velocities of exospheric atoms relative to the Sun should be taken into account to more accurately estimate the emitting column density from radiance observations. A summary of our findings is given in Section 4.

## 2. The Photon Scattering Coefficient and Radiation Acceleration

### 2.1. Radiation Acceleration Basics

UVVS observed emission produced by resonant scattering of sunlight, the process by which photons at wavelengths corresponding to resonant transitions in an atom are absorbed and quickly reemitted. The resonant scattering rate (photons  $\text{atom}^{-1} \text{s}^{-1}$ ) is given by the photon scattering coefficient,  $g$ , the product of the incident photon flux at the resonant wavelength and the scattering probability per atom (J. W. Chamberlain 1961). In this section, we show how variations in  $g$  as a function of Mercury’s heliocentric distance and radial velocity with respect to the Sun affect the structure of Mercury’s exosphere and escape rates into the tail.

Because incident photons originate from the direction of the Sun and are emitted approximately isotropically, there is a change in the total momentum of the photons. This momentum is imparted to the atoms, resulting in a net force. The radiation acceleration ( $a_r$ , force per unit mass) is given approximately<sup>7</sup> by

$$a_r = \sum_i g_i(v_{\rho\odot}) \times \frac{h}{m\lambda_i}, \quad (1)$$

where  $g$  is the photon scattering coefficient (hereafter referred to as the  $g$ -value) at the resonant wavelength  $\lambda_i$  in the rest frame of the absorbing atom;  $v_{\rho\odot} = dr_{\odot}/dt$  is the radial velocity of the atom relative to the Sun, where  $r_{\odot}$  is the radial distance from the Sun and  $t$  is time;  $h$  is Planck’s constant;  $m$  is the mass of the absorbing atom; and the sum is over all resonant transitions  $i$  (W. H. Smyth 1979; J. W. Chamberlain & D. M. Hunten 1987). The  $g$ -value depends on the number of

photons available at the resonant wavelengths in the atom’s rest frame because the corresponding Doppler-shifted solar flux varies with wavelength. The  $g$ -values of resonance lines of atoms relevant for studies of Mercury’s exosphere have been calculated as functions of  $v_{\rho\odot}$  using high-resolution solar spectra (R. Killen et al. 2009a, 2009b; R. M. Killen et al. 2022).

Figure 1(a) shows the magnitude of the radiation acceleration for Na, Mg, and Ca as functions of  $v_{\rho\odot}$  at a distance of 0.39 au (Mercury’s semimajor axis). Table 1 lists the masses and resonant wavelengths for the atoms shown in Figure 1. Figure 1(b) shows the magnitude of  $a_r$  for atoms at rest relative to Mercury as a function of Mercury’s TAA. The solar flux at these wavelengths varies over a Mercury year for two reasons. First, Mercury receives 44% of the flux at aphelion ( $r_{\odot} = 0.47$  au) that it receives at perihelion ( $r_{\odot} = 0.31$  au) because of its elliptical orbit. Second, absorption of sunlight in the solar atmosphere creates broad absorption features in the solar spectrum (Fraunhofer absorption lines). For Na and Ca, this results in 1 order of magnitude variation in  $a_r$  over the course of a mercurian year for an atom at rest relative to Mercury. The peak  $a_r$  of Na for an atom at rest relative to Mercury is  $\sim 0.5$  times Mercury’s surface gravitational acceleration of  $370 \text{ cm s}^{-2}$ . Mg shows only a factor of  $\sim 2$  variation in  $a_r$  and will not be considered further in this work.

### 2.2. Radiation Acceleration and Exospheric Escape

#### 2.2.1. Na

Neutral atoms launched from Mercury’s surface can either escape, be photoionized and picked up by the solar wind or the planetary magnetic field (N. Meyer-Vernet 2009), or return to the surface (if not ionized or escaped). An atom is deemed to have escaped Mercury if its speed is greater than the escape speed from Mercury at the atom’s distance and if its distance from Mercury is increasing, with a check performed to ensure that atoms ejected toward the Sun faster than the escape speed but pushed back to the surface are not counted as having escaped. For simplicity, we have assumed that atoms that return to the surface stick with 100% efficiency. Because these represent the range of possible outcomes for an atom that is launched from the surface,  $f_{\text{esc}} + f_{\text{hit}} + f_{\text{ion}} \equiv 1$ , where  $f_{\text{esc}}$  is the fraction that reaches escape speed,  $f_{\text{hit}}$  is the fraction that returns to the surface, and  $f_{\text{ion}}$  is the fraction that is photoionized before escaping or hitting the surface. Particle trajectories were computed using an updated version of the Monte Carlo model used by M. H. Burger et al. (2014; M. Burger 2025).

Figure 2 shows variations in  $f_{\text{esc}}$ ,  $f_{\text{hit}}$ , and  $f_{\text{ion}}$  as functions of TAA, for four Na surface sources with and without radiation pressure. These sources are not intended to represent the range of possible source mechanisms operating at Mercury but to simulate a diverse set of initial conditions. Panels (a) and (b) simulate monoenergetic source functions with atoms launched isotropically from the surface at fixed speeds of 2 and  $4 \text{ km s}^{-1}$ , well below and close to the  $4.25 \text{ km s}^{-1}$  escape velocity at Mercury’s surface, respectively. Panels (c) and (d) use sources more representative of actual source processes at Mercury. Figure 2(c) simulates a Na source with a 1200 K Maxwellian flux distribution that is uniform over Mercury’s dayside. Atoms are ejected isotropically into the  $2\pi$  steradians outward-directed hemisphere. This is consistent with the

<sup>7</sup> Polarization of the scattered wave can cause a small asymmetry in the phase function in emitted light that affects brightness, although the correction factors are near unity and can be ignored (J. W. Chamberlain 1961; J. W. Chamberlain & D. M. Hunten 1987). Because the phase functions are symmetric with equal forward- and backscattered amounts, this does not affect the momentum balance.

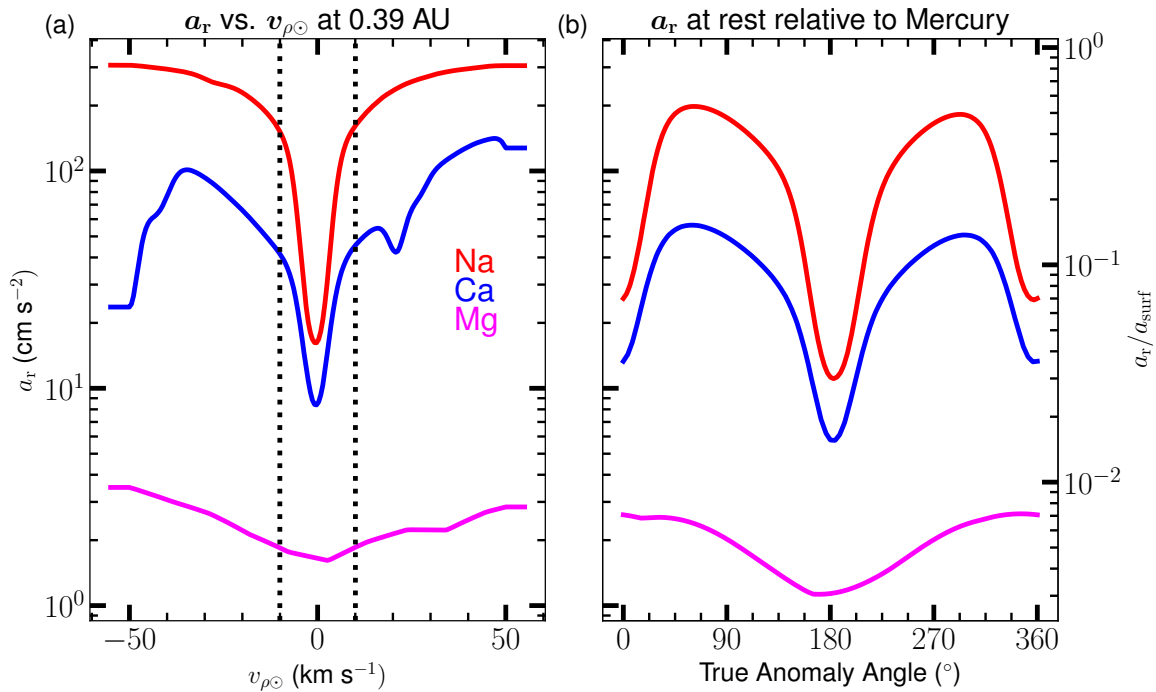


**Figure 1.** (a) Radiation acceleration ( $a_r$ ) for Na (red), Mg (magenta), and Ca (blue) as a function of radial velocity relative to the Sun ( $v_{\rho_{\odot}}$ ) at a solar distance of 0.39 au. The dotted lines show  $\pm 10$   $\text{km s}^{-1}$ , Mercury’s minimum and maximum radial velocity relative to the Sun. (b)  $a_r$  of the same species as a function of Mercury’s true anomaly angle (TAA) for an atom at rest relative to Mercury. The scale on the left shows the magnitude of the  $a_r$  near Mercury. The scale on the right shows for both (a) and (b) the ratio of the radiation acceleration to the surface gravitational acceleration.

**Table 1**  
Atomic Species Included in Model Simulations

Species	Mass (AMU)	Resonant $\lambda$ ( $\text{\AA}$ )
Na	23.0	5891.6, 5897.6
Mg	24.3	4227.9
Ca	40.1	2853.0

**Note.** The resonant wavelengths are vacuum wavelengths.

1200 K atmospheric scale height measured by UVVS (T. A. Cassidy et al. 2015) and inferred from seasonal variations in the tail (T. A. Cassidy et al. 2021). Doppler widths of resolved emission line profiles also support a 1200 K Na source (R. M. Killen et al. 1999; P. Lierle et al. 2022). The source flux is taken to be uniform over the dayside both for simplicity and because it is consistent with the PSD source in the absence of ion precipitation found by M. H. Burger et al. (2010), who argued the source flux from the surface was approximately constant over the dayside because it was limited by the diffusion rate of Na to grain surfaces, not by the solar photon flux. Figure 2(d) uses a 3500 K source centered on the dawn (orbital ram) hemisphere that is consistent with model predictions of an MIV source (P. Pokorný et al. 2017; R. M. Killen et al. 2018). The thermal speeds,  $v_{\text{th}}$ , of Na at 1200 and 3500 K are 0.9 and 1.6  $\text{km s}^{-1}$ , respectively.

As shown in Figure 2(a), if all Na atoms were ejected from the surface at 2  $\text{km s}^{-1}$  and there were no radiation pressure or photoionization, all particle trajectories would begin and end at the surface. Adding in photoionization,  $\sim 3\%$  of neutral atoms are lost before hitting the surface when averaged over TAA. The variations in  $f_{\text{hit}}$  and  $f_{\text{ion}}$  are due to the  $r^{-2}$  dependence of the photoionization rate, which reflects the inverse-square law

governing solar flux with distance from the Sun. When radiation pressure is included, a tail would form between TAA  $\sim 33^{\circ}$  and  $103^{\circ}$ , with a peak escape fraction of neutral atoms of  $\sim 0.06$  at TAA =  $62^{\circ}$ . A small amount of additional escape ( $\lesssim 10^{-3}$ ) happens between TAA  $\sim 281^{\circ}$  and  $296^{\circ}$ . At all other TAAs, the escape fraction of neutral atoms is 0. Almost all of the escaping neutral atoms would have hit the surface without radiation pressure;  $f_{\text{ion}}$  remains largely unchanged.

Considering the 4  $\text{km s}^{-1}$  simulation (Figure 2(b)), when radiation pressure is not included, no neutral Na atoms escape, and the  $f_{\text{hit}}$  and  $f_{\text{ion}}$  vary with heliocentric distance as in the 2  $\text{km s}^{-1}$  simulation. However, because the mean time to return to the surface is much longer when launched at 4  $\text{km s}^{-1}$  than at 2  $\text{km s}^{-1}$  (12.8 and 0.4 hr, respectively),  $\sim 90\%$  of the faster Na is ionized. When radiation pressure is included,  $\sim 80\%$  of atoms launched escape when averaged over a Mercury year, despite being launched below the escape speed.

With the 1200 K dayside Na source, shown in Figure 2(c), we find that some neutral Na is able to escape when radiation pressure is included, even though there are few launched above escape velocity. In this simulation, escape occurs at nearly all TAAs except near perihelion and aphelion, with peak escape fractions of  $f_{\text{esc}} = 1.3 \times 10^{-2}$  at TAA =  $58^{\circ}$  and  $0.7 \times 10^{-2}$  at TAA =  $285^{\circ}$ .

Lastly, in Figure 2(d), the escape fraction for the 3500 K source shows similar trends to the 1200 K source, although the escape fraction is  $> 0.01$  for all TAAs, and the maxima are shifted toward later TAAs. The maximum escape fraction of neutral atoms is 0.22 at  $64^{\circ}$  on the outbound portion of the orbit and 0.19 at  $291^{\circ}$  on the inbound portion. As with the 4  $\text{km s}^{-1}$  source, the minima occur just before perihelion and just after aphelion.

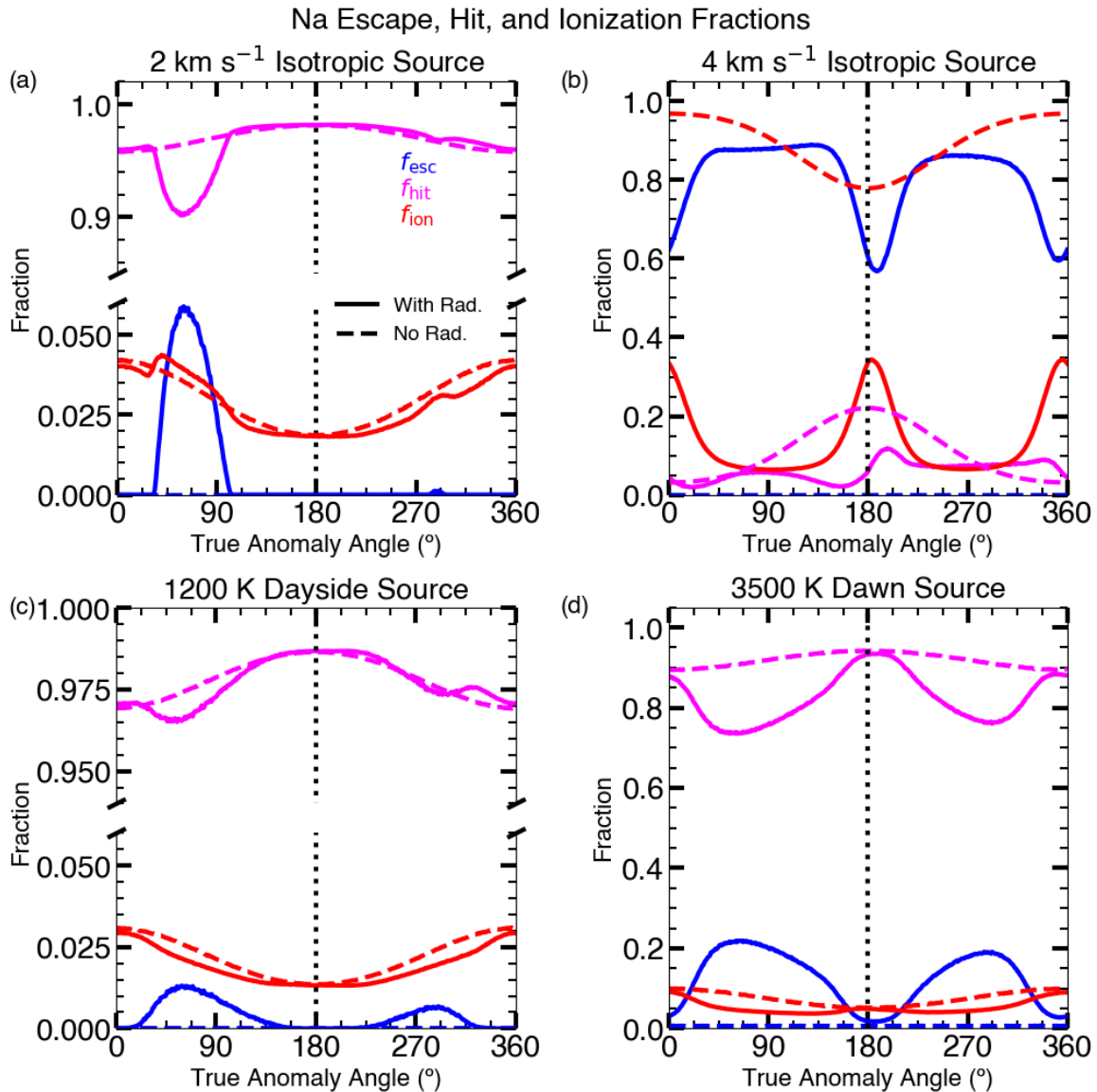


**Figure 2.** The fractions  $f_{\text{esc}}$  (blue),  $f_{\text{hit}}$  (magenta), and  $f_{\text{ion}}$  (red) as a function of Mercury’s TAA. The solid lines include radiation pressure; radiation pressure is turned off for the dashed lines. The black dotted line indicates aphelion. (a) Na atoms are ejected isotropically from Mercury at  $2 \text{ km s}^{-1}$ . (b) Na atoms are ejected isotropically at  $4 \text{ km s}^{-1}$ . (c) Source is a  $1200 \text{ K}$  Maxwellian flux distribution isotropic on Mercury’s dayside. (d) Source is a  $3500 \text{ K}$  Maxwellian flux distribution centered on Mercury’s dawn equatorial point. The y-axes in panels (a) and (c) have gaps to highlight the behavior of the curves at values near zero and one.

Without radiation pressure, no neutral atoms from the  $1200 \text{ K}$  source escape. With the  $3500 \text{ K}$  source,  $\sim 1\%$  of atoms are ejected above the escape speed.

There are two asymmetries in the escape fraction as a function of TAA that are apparent from Figure 2. In the following discussion, we focus on the  $4 \text{ km s}^{-1}$  source as the variations with TAA are largest, but the conclusions apply to some extent to all four initial source distributions used.

The first asymmetry is of the broad peaks between  $\text{TAA} \sim 40^\circ$  and  $140^\circ$  on the outbound portion of Mercury’s orbit (from perihelion to aphelion,  $0^\circ \leq \text{TAA} < 180^\circ$ , when Mercury’s distance from the Sun is increasing) and between  $\text{TAA} \sim 230^\circ$  and  $310^\circ$  on the inbound portion (aphelion to perihelion,  $180^\circ \leq \text{TAA} < 360^\circ$ , when Mercury’s distance from the Sun is decreasing). The escape fraction is slightly greater when Mercury is outbound than inbound. On average,  $84\%$  of the Na escapes when Mercury is moving away from the Sun compared with  $77\%$  when moving toward the Sun.

The second asymmetry is that the minima in  $f_{\text{esc}}$  are not aligned with the minima in radiation pressure, but instead occur just before perihelion and just after aphelion. The asymmetries seen in  $f_{\text{ion}}$  roughly mirror those seen in  $f_{\text{esc}}$ . There are peaks just before perihelion and just after aphelion, and broad minima at the same TAAs where  $f_{\text{esc}}$  peaks. The variations in  $f_{\text{hit}}$ , detailed below, are more complicated, but also show maxima before perihelion and after aphelion.

These annual asymmetries are due to variations in the time atoms remain in the exosphere over the course of a Mercury year. In the model, particle trajectories are computed, with the number of atoms that a test particle represents decreasing over time due to photoionization. Therefore, each trajectory represents atoms that either escape or return to the surface, and atoms that are photoionized along the trajectory. Every trajectory in this sense is either escaping or bound, even though atoms along the trajectory might be photoionized. Figure 3 shows how the mean length of time an atom remains

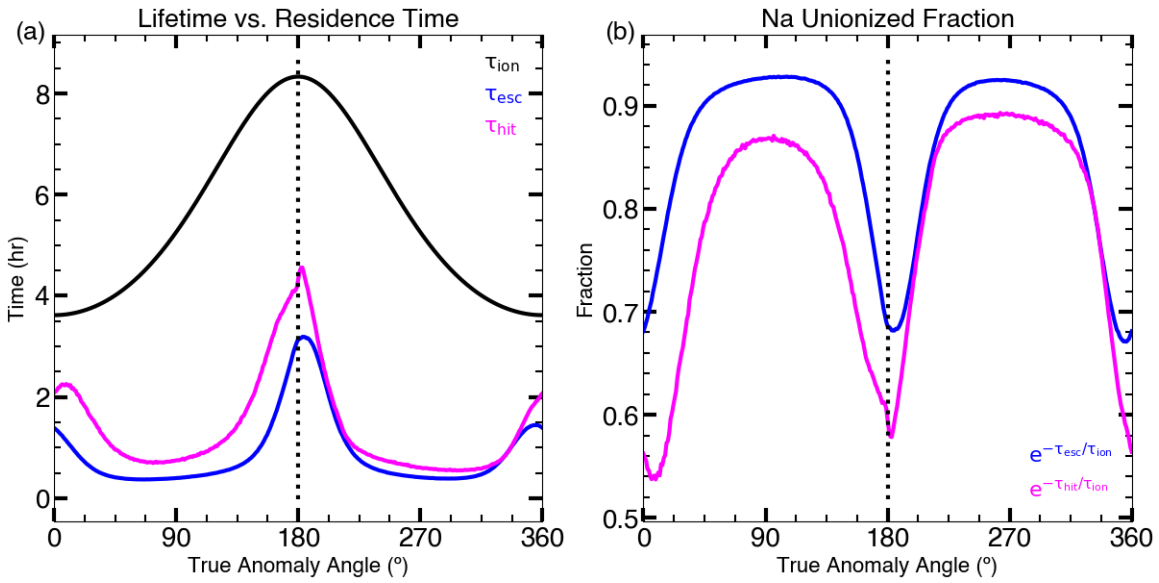


**Figure 3.** (a) The photoionization lifetime  $\tau_{\text{ion}}$  (black), and mean residence times  $\tau_{\text{esc}}$  (blue) and  $\tau_{\text{hit}}$  (magenta) for atoms to reach escape speed or return to the surface, respectively, for atoms ejected from the surface at  $4 \text{ km s}^{-1}$ . (b) Fractions of atoms along escaping trajectories that reach escape speed (blue) and along bound trajectories that return to the surface (magenta).

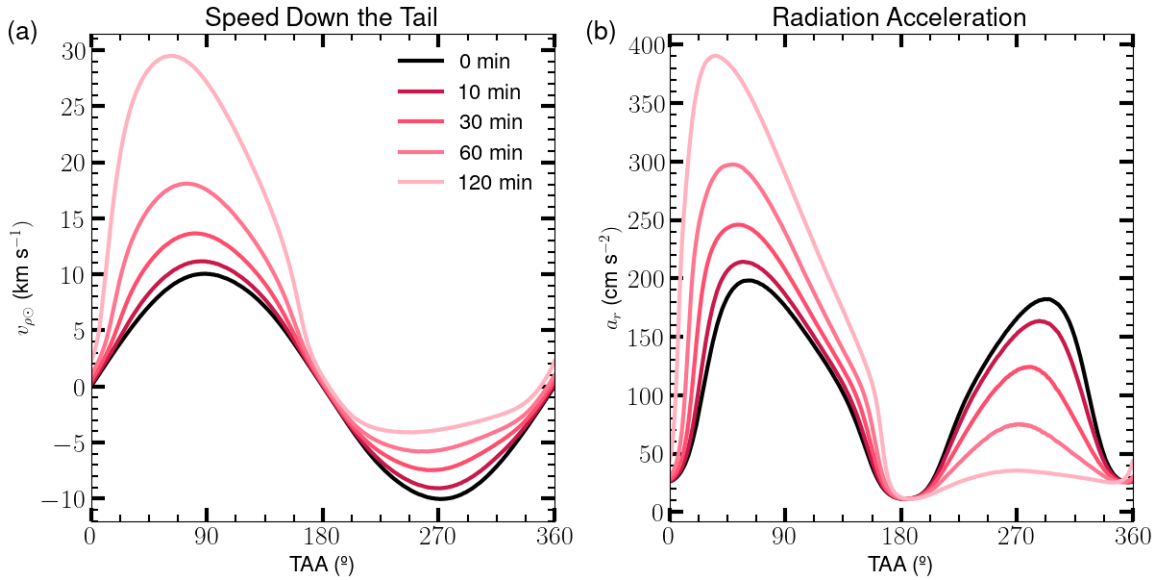


**Figure 4.** (a)  $v_{p_{\odot}}$  of an atom initially at rest relative to Mercury as functions of TAA and time since the atom was launched from the surface. The black line represents  $t = 0 \text{ s}$ , with lighter shades of red indicating longer travel times from 10 to 120 minutes. The only force acting on the atom is radiation pressure. (b)  $a_r$ , as functions of time and TAA acting on the same atom.

in the exosphere affects the fraction of atoms that escape or return to the surface. The simulations were completed with a  $4 \text{ km s}^{-1}$  isotropic source from the surface because it shows the effects more clearly and because it reduces the number of variables that could be affecting the results. By using a monoenergetic, spatially isotropic source, we can more clearly demonstrate that the asymmetries we see are not due to the details of the spatial or energy distributions. The residence times are the mean time it takes atoms to either escape ( $\tau_{\text{esc}}$ ) or return to the surface ( $\tau_{\text{hit}}$ ). These are given, along with the photoionization lifetime ( $\tau_{\text{ion}}$ ), in Figure 3(a) as functions of TAA. The fraction of atoms that have not been ionized after time  $t$  is given by  $e^{-t/\tau_{\text{ion}}}$ . Figure 3(b) shows the unionized fraction of escaping and bound atoms after  $\tau_{\text{esc}}$  and  $\tau_{\text{hit}}$ ; i.e.,

these represent the fraction of atoms that escape or hit the surface. These show broadly the same asymmetries seen in Figure 2.

These effects can be explained by feedback loops in the system (A. E. Potter et al. 2007). Figure 4 shows how the radial velocity and magnitude of the radiation pressure vary over time for a Na atom initially at rest relative to Mercury. Mercury's gravity is not included in this. Panel (a) shows how an atom's radial velocity evolves over 120 minutes when starting at rest. On the outbound part of the orbit, Mercury is moving away from the Sun. Radiation pressure always increases the magnitude of  $v_{p_{\odot}}$ , and in a positive feedback loop, the radiation acceleration also increases, as shown in Figure 4(b). On the inbound portion, the direction of radiation

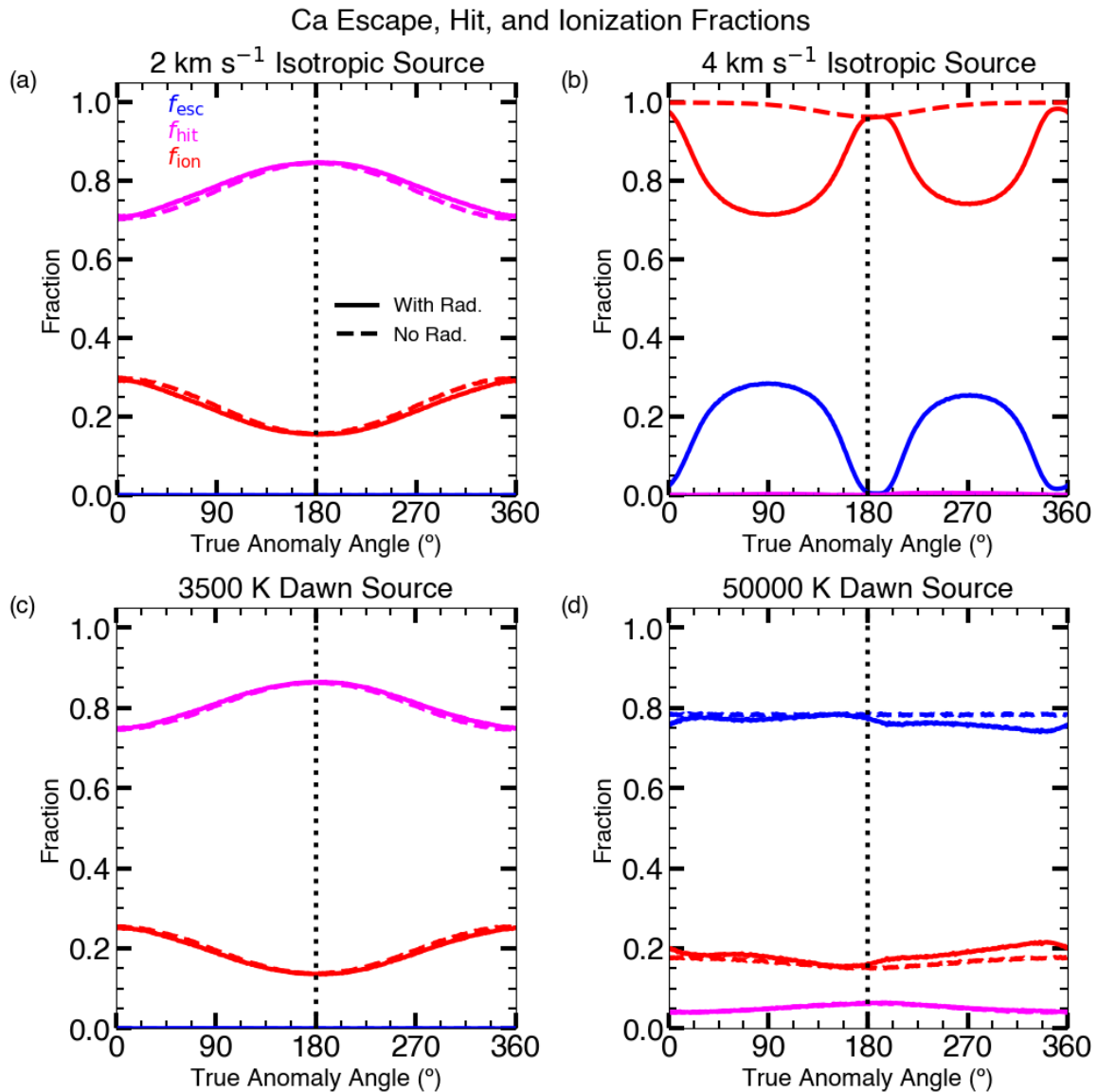


**Figure 5.** The fractions  $f_{\text{esc}}$  (blue),  $f_{\text{hit}}$  (magenta), and  $f_{\text{ion}}$  (red) as a function of Mercury's TAA. Solid lines include radiation pressure; radiation pressure is not included in the models shown by the dashed lines. The dotted line indicates aphelion. (a) Ca atoms are ejected isotropically from Mercury at 2 km s<sup>-1</sup>. (b) Ca atoms are ejected isotropically at 4 km s<sup>-1</sup>. (c) Source is a 3500 K Maxwellian flux distribution centered on Mercury's dawn equatorial point. (d) Source is a 50,000 K Maxwellian flux distribution centered on Mercury's dawn equatorial point.

pressure is acting opposite to the direction of motion, creating a negative feedback loop. The atom slows down over time while it is moving toward the Sun, and consequently, the magnitude of radiation pressure decreases. As a result, atoms are more likely to reach escape speed before being photoionized when Mercury is moving away from the Sun than toward it.

### 2.2.2. Ca

The behavior for Ca, as shown in Figure 5, is quite different from Na. Panels (a) and (b) show the same 2 and 4 km s<sup>-1</sup> monoenergetic sources as in Figures 2(a) and (b). Panels (c) and (d) use Maxwellian flux distributions centered on the dawn hemisphere at 3500 K to simulate production of atomic Ca by MIV, and 50,000 K, respectively, the latter consistent with the source derived from the analysis of UVVS data (M. H. Burger et al. 2012, 2014). Although the precise temperature and

energy distribution of Ca are uncertain, the modeling by M. H. Burger et al. (2014) indicated that the bulk of the Ca must be ejected above the escape speed. The exact speed distribution function had little effect on the results (i.e., any distribution with mostly escaping Ca would have looked similar to UVVS).

The differences between Na and Ca arise from a combination of weaker radiation pressure acting on Ca (see Figure 1) and a shorter photoionization lifetime for Ca relative to Na. The neutral lifetime of Ca varies between 23 and 52 minutes, whereas the Na lifetime varies between 3.6 and 8.3 hr, respectively, from perihelion and aphelion (based on the ionization rates from W. F. Huebner & J. Mukherjee 2015).

Because of the short photoionization lifetime for neutral Ca, ionization plays the defining role in shaping the Ca exosphere rather than radiation pressure. Except for atoms launched near the escape speed (e.g., 4 km s<sup>-1</sup>), there is little difference between the exosphere with and without radiation pressure.

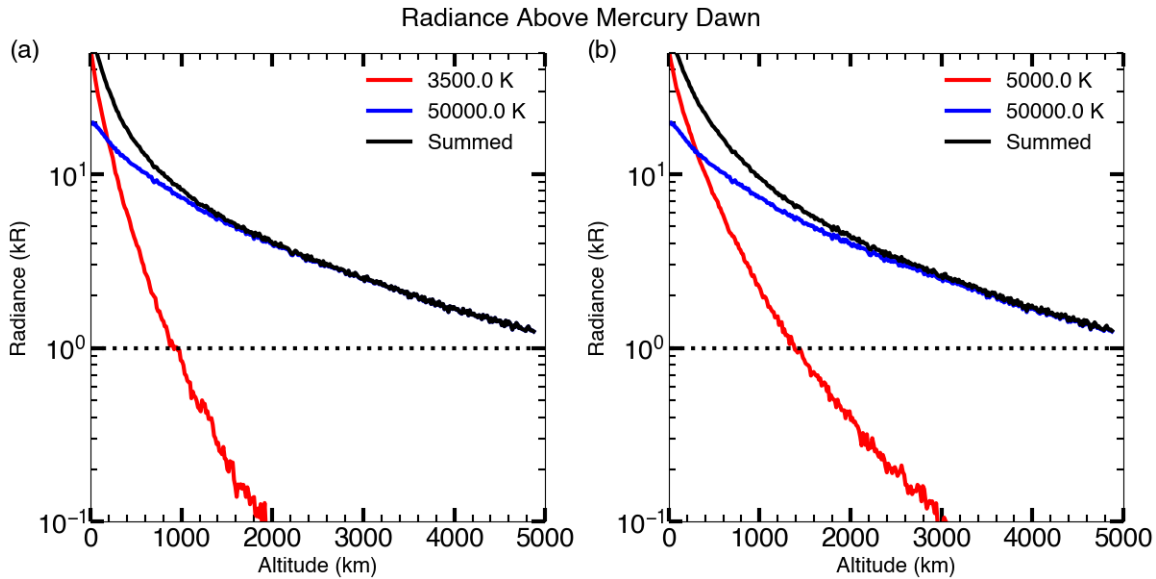


**Figure 6.** The Ca radiance as a function of altitude. (a) A 3500 K source is shown in red, a 50,000 K source in blue, and the sum of the two profiles is the solid black line. The dotted line indicates the approximate 1 kR detection limit for Ca by UVVS. (b) Same as (a) with a 5000 K source in place of a 3500 K source.

For the  $4 \text{ km s}^{-1}$  source, up to 28% of Ca reaches escape speed when  $v_{\rho\odot}$  is large (TAA  $\sim 90^\circ$  and  $270^\circ$ ), and a small fraction ( $\sim 0.3\%$ ) escapes when  $v_{\rho\odot}$  is near  $0 \text{ km s}^{-1}$  (TAA  $\sim 0^\circ$  and  $180^\circ$ ). With the 3500 K source ( $v_{\text{th}} = 1.2 \text{ km s}^{-1}$ ),  $f_{\text{esc}} \lesssim 10^{-3}$  everywhere along the orbit, with 80% of Ca, on average, returning to the surface and the rest being ionized. With the 50,000 K source ( $v_{\text{th}} = 4.6 \text{ km s}^{-1}$ ), most atoms are ejected above the escape speed, which reduces the dependence of the photoionization rate on the escape fraction.

In Figure 6, we look at the detectability of a cold MIV source. The radiance from sources at 3500 K (red, panel (a)), 5000 K (red, panel (b)), and 50,000 K (blue, both panels) as a function of altitude above Mercury’s dawn point is shown for an observer looking perpendicular to the equatorial plane from above. Mercury’s TAA is  $90^\circ$ . The solid black lines give the sum of the two sources in each panel. The dotted black lines show the approximate 1 kR detection threshold for Ca in the UVVS data. We have assumed equal source rates of  $2 \times 10^{23} \text{ atoms s}^{-1}$  for each source. Modeling suggests that most Ca ejected by impact vaporization is in molecular form (A. A. Berezhnoy & B. A. Klumov 2008; A. A. Berezhnoy 2018), a prediction supported by the lack of an observed atomic Ca component from a likely impact event that increased the exospheric Na and Mg abundances (T. A. Cassidy et al. 2021). Therefore, using equal source rates gives an upper limit on the radiance of the cold source relative to the hot source.

We conclude that it would have been difficult to detect a cold Ca source in the UVVS dataset. On the dayside, much of the data below  $\sim 500 \text{ km}$  is dominated by scattered sunlight. While the cold sources are brighter than the hot source very close to the surface, at 500 km altitude, the 50,000 K source is 2.7 and 1.5 times the 3500 K and 5000 K sources, respectively, with the cold source dropping in brightness much faster than the hot source. We note that this analysis is not a precise look at the UVVS performance because we did not take into account the full details of the UVVS observing geometry, but it does give an order-of-magnitude sense of the relative detectability of colder sources.

### 2.3. Effect of Radiation Acceleration on Understanding Exospheric Sources

Radiation pressure can often cause confusion as to where atoms originated on Mercury’s surface. This effect is strong for Na, but less important for Ca due to the short photoionization lifetime. Figure 7 shows trajectories of Na atoms ejected into the equatorial plane from the dayside at 2 (left) and  $4 \text{ km s}^{-1}$  (right); there is no motion in the north/south direction. We limited the simulation to two dimensions for clarity in showing the results. Particles are ejected isotropically from the dayside into all directions in the equatorial plane. Each panel shows either escaping or bound trajectories for three different TAA:  $0^\circ$ ,  $90^\circ$ , and  $290^\circ$ , corresponding to perihelion, maximum outbound velocity, and inbound motion near peak escape flux, respectively. For each TAA/speed combination, escaping trajectories are shown on the left; bound trajectories are on the right. Black trajectories escape down the tail, but are also pulled strongly enough by gravity when near the surface to wrap around the nightside and cross the Sun–Mercury line (SML). Red trajectories also escape down the tail, but do not cross the SML. The blue trajectories begin and end on Mercury’s dayside. Those in magenta begin on the dayside and get pushed antisunward, but do not reach escape velocity and fall to the surface on the nightside.

Table 2 shows the fraction of trajectories that fall into each of four categories: escaping and crossing the SML, escaping and not crossing the SML, bound and hitting the dayside, and bound and hitting the nightside. We have used a full three-dimensional simulation with Na atoms ejected isotropically from the dayside instead of the two-dimensional simulation used for Figure 7. Ionization is not taken into account in these results; i.e., the numbers reflect the fraction of trajectories that are bound or escaping, not the number of neutral atoms on such trajectories.

At perihelion, radiation acceleration is minimal. Atoms ejected at  $2 \text{ km s}^{-1}$  are unable to travel far from their source and all of them return to the surface, mostly (85%; see Table 2) on the dayside. At  $4 \text{ km s}^{-1}$ , despite the atoms launching

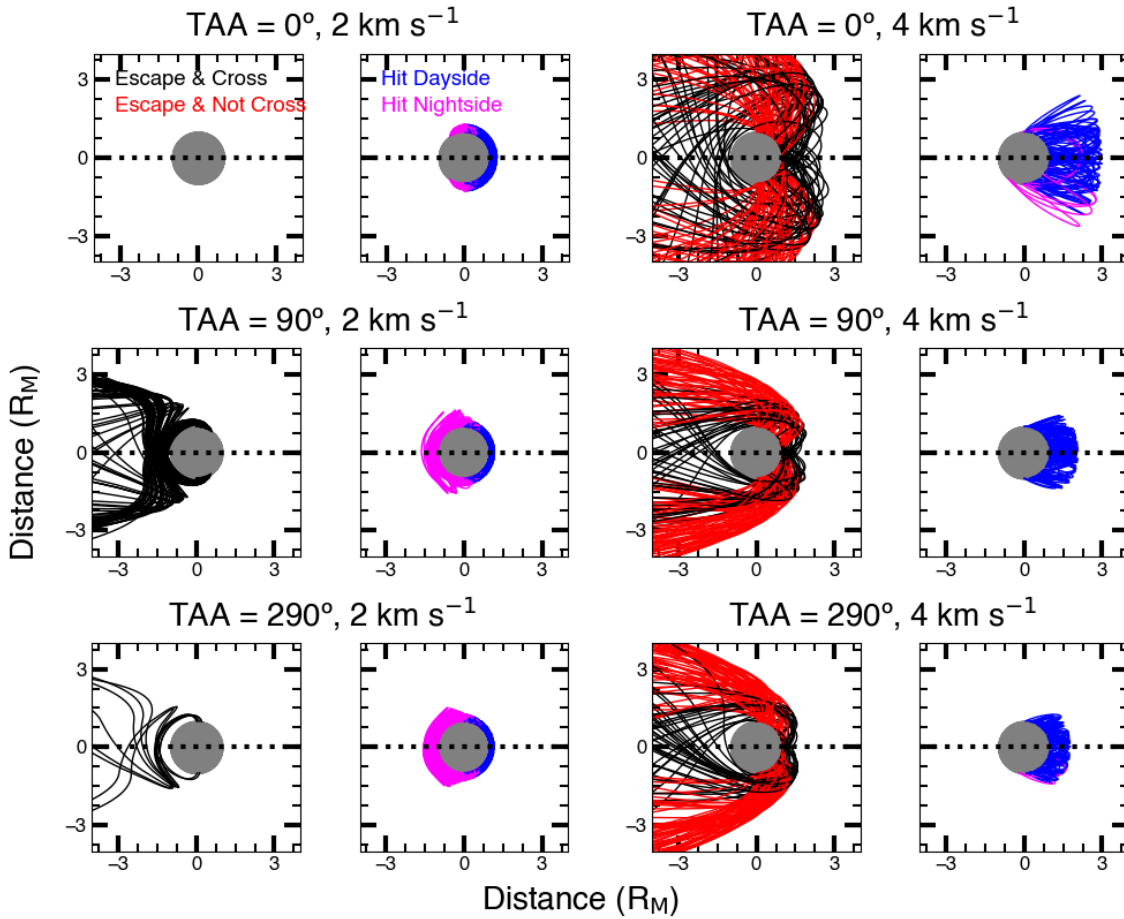


**Figure 7.** Trajectories of Na atoms ejected isotropically in the equatorial plane from Mercury’s dayside. Top row: TAA = 0°. Middle row: TAA = 90°. Bottom row: TAA = 290°. Left pair of panels:  $v_0 = 2 \text{ km s}^{-1}$ . Right pair of panels:  $v_0 = 4 \text{ km s}^{-1}$ . For each pair of panels, the left panel shows escaping trajectories and the right shows bound trajectories. Escaping trajectories that cross the SML are shown in black and those that do not cross the SML are shown in red. Blue trajectories begin and end on the dayside. Magenta trajectories begin on the dayside and end on the nightside.

**Table 2**  
End State of Na Trajectories Launched from Mercury’s Surface

TAA (deg)	Speed (km s <sup>-1</sup> )	Escape and		Hit Dayside (%)	Hit Nightside (%)
		Cross SML (%)	Not Cross SML (%)		
0	2	0.0	0.0	85.2	14.8
0	4	52.1	42.0	4.6	1.4
90	2	4.6	0.0	76.1	19.3
90	4	41.6	50.4	7.6	0.3
290	2	0.2	0.0	75.9	23.9
290	4	41.6	46.3	11.4	0.6

slower than escape velocity, 94% of the trajectories are escaping due to the effects of radiation acceleration. The only bound trajectories are those directed primarily toward the Sun (i.e., having small dawn–dusk or north–south velocity components) such that when radiation pressure pushes them back, they are not able to clear the planet’s limb. A bit more than half (55%) of the escaping trajectories cross the SML. These are close to the planet after being pushed back by radiation pressure so that Mercury’s gravity is strong enough to affect the trajectories but not strong enough to retain the atoms.

At TAA = 90°, where Mercury’s radial velocity is maximal, 4% of the 2 km s<sup>-1</sup> Na trajectories escape, with the rest returning to the surface. All escaping trajectories cross the SML, typically originating near the terminator and initially directed mostly perpendicular to the SML. For the 4 km s<sup>-1</sup> source, a smaller fraction of Na trajectories cross the SML, with ~45% of the escaping Na ending up on the opposite side of the planet from which it was ejected.

At TAA = 290°, for 2 km s<sup>-1</sup>, the results resemble the trajectories at 90°, except that 99.8% of Na atoms are launched on bound trajectories, and the ratio of trajectories hitting the dayside to those hitting the nightside decreased from 3.9 to 3.4. All of the escaping trajectories cross the SML. For 4 km s<sup>-1</sup>, the number of escaping trajectories decreased by ~4 percentage points from TAA = 90° to 290°, with all the now-bound trajectories having been non-SML crossing trajectories that now hit the dayside. This reflects the negative feedback loop discussed earlier: atoms moving toward the Sun are decelerated, reducing their chance of reaching escape speed before being pulled back.

The net forces acting on atoms are symmetric about the SML, while the simulations in Figure 7 were in the equatorial plane. The same conclusions would apply to any plane containing the SML, such that, for example, Na ejected from southern regions might be more easily observed over the

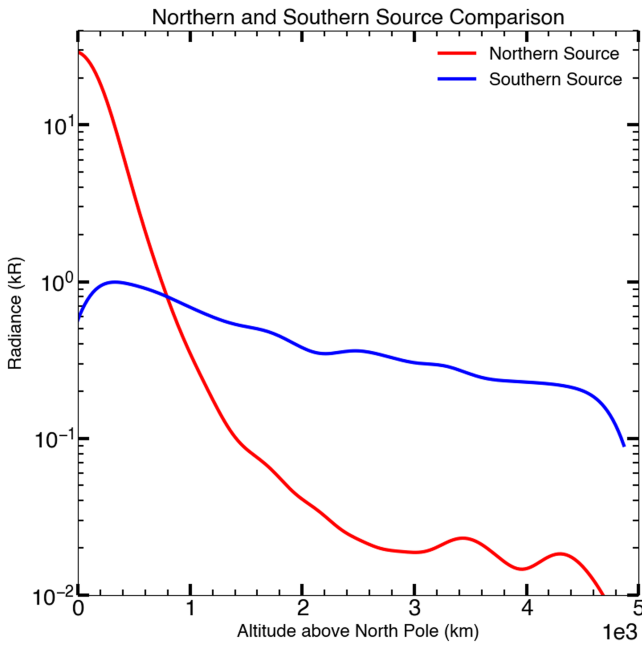


**Figure 8.** Altitude profiles over Mercury’s north pole for 1200 K sources that are uniform over the dayside northern hemisphere (red) and the dayside southern hemisphere (blue).

north pole of the planet. This is demonstrated in Figure 8, which shows altitude profiles above the north pole for two simple 1200 K source distributions: one that is uniform on the dayside northern hemisphere source and one that is uniform on the dayside southern hemisphere. Below  $\sim 800$  km altitude, the northern source dominates the brightness. At higher altitudes, however, material ejected from the southern hemisphere produces more emission over the north pole than the more localized source. This shows that radiation pressure can distort the view of where on the surface material originates.

### 3. Effect of Variable $g$ -value on Resonant Scattering Emission

The column density  $N$  along a line of sight is the integrated density:

$$N = \int_0^{\infty} n(s) ds, \quad (2)$$

where  $n(s)$  is the number density at a distance  $s$  from the observer, and the integral is taken along the line of sight. The radiance of a column of a resonantly scattering gas is

$$I = 10^{-9} \int_0^{\infty} g(v_{\rho\odot}) n(s) ds, \quad (3)$$

where  $I$  is the radiance,  $g(v_{\rho\odot})$  is the  $g$ -value for the differential density element taking into account the Doppler shift in the rest wavelength relative to the Sun of the differential element, and the integral is along the line of sight. The factor of  $10^{-9}$  puts the radiance in the units kR, where 1 kR is the emission from  $10^9$  photons emitted per second isotropically, provided that the density is in  $\text{cm}^{-3}$  and  $g(v_{\rho\odot})$  is in  $\text{photons s}^{-1}$ . In these test particle simulations, we count the number of

particles along the line of sight such that

$$N = \sum_i \eta_i / A, \quad (4)$$

$$I = \sum_i 10^{-9} \eta_i g_i(v_{\rho\odot}) / A, \quad (5)$$

where  $\eta_i$  is the number of atoms that each test particle represents and is assumed to be distributed over a column with area  $A$  (e.g., the area of a pixel in an image or the cross sectional area of the projected UVVS observing slit). The  $g$ -value,  $g_i(v_{\rho\odot})$ , for each test particle is determined using the  $v_{\rho\odot}$  tracked in the model.

Here, we will show that it is generally not appropriate to simply use the Mercury-at-rest  $g$ -value for determining the emitting column density of gas using only the radiance. If the  $g$ -value is taken as a constant, then Equation (5) simplifies to

$$\tilde{I} = 10^{-9} N g_M, \quad (6)$$

where  $\tilde{I}$  is the approximate radiance and  $g_M$  is the  $g$ -value for an atom at rest relative to Mercury. Equation (6) will often lead to an over- or underestimate of the emitting column density, as demonstrated in Figures 9 and 10. These figures compare model outputs for a 1200 K dayside Na source and a 50,000 K dawn-centered Ca source, respectively. The viewing geometry is from above Mercury’s north pole, with the  $x$ -axis pointing toward the Sun and the  $y$ -axis toward dusk. Each figure presents, from top to bottom: (1) modeled radiance assuming a source rate of  $10^{23}$  atoms  $\text{s}^{-1}$ ; (2)  $N$ , the column density determined directly from the model; (3)  $\tilde{N}$ , the approximate column density inferred from the modeled radiance, i.e., the inverse of Equation (6) ( $\tilde{N} = \frac{10^9 I}{g_M}$ ); and (4) the ratio  $\tilde{N}/N$ . Red regions indicate where the constant- $g$  assumption leads to an overestimate of the column density, while blue regions indicate underestimates. The source rate does not affect the comparison, as both radiance and column density scale linearly with it. The column density enhancement on the night side seen for Na at  $90^\circ$  and  $290^\circ$  is a result of  $\sim 20\%$ – $25\%$  of the Na being transported to the night side while still being bound to Mercury (Section 2.3). This enhancement does not show up in the corresponding radiance images because the atoms are in Mercury’s geometric shadow.

For both sources, there is a clear effect on the derived column density from the radiance using  $g_M$  instead of the  $g$ -values that take into account how the radial velocity of atoms relative to the Sun varies with both location relative to Mercury and with Mercury TAA. At perihelion (left columns), using  $g_M$  results in an overestimate of the column density everywhere except directly antisunward of Mercury, where radiance is reduced due to atoms in Mercury’s shadow being undetectable. The column density is overestimated everywhere else because  $g_M$  is at its minimum and  $g(v_{\rho\odot})/g_M \geq 1$  everywhere ( $\tilde{N} \sim g(v_{\rho\odot})/g_M$ ). The effect is stronger for Ca than Na because 50,000 K Ca is moving much faster relative to Mercury than the 1200 K Na.

On the outbound portion of the orbit (TAA =  $90^\circ$ , middle columns), the column density is overestimated on the nightside

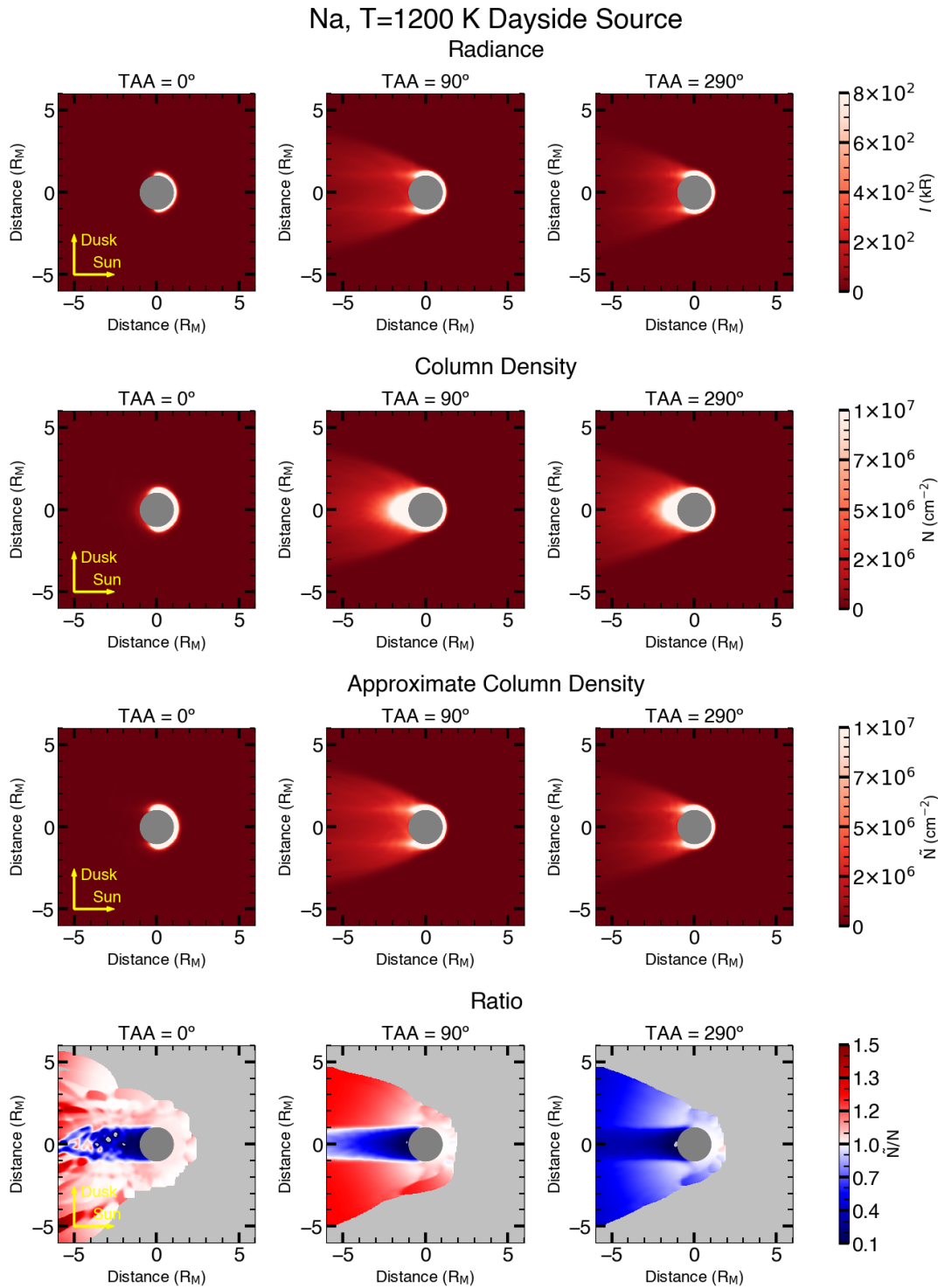


**Figure 9.** Model images of a 1200 K, dawn-centered Na source. Top Row: modeled radiance at TAA = 0° (left), 90° (middle), and 290° (right). Second row: column density ( $N$ ) taken from the model at the same TAAs. Third Row: approximated column density ( $\tilde{N}$ ) determined by the inverse of Equation (6). The color scales for the second and third rows are the same. Bottom row:  $\tilde{N}/N$ . Regions with no Na present are shown in light gray. The stretch of the colorbar in the last row is not symmetric for values greater than and less than 1.

for both species and, for Ca, underestimated on the dayside.<sup>8</sup> This happens because of the feedback loop discussed above. Na and Ca atoms on Mercury’s nightside get accelerated by

<sup>8</sup> The dayside Na results are less significant, as very little Na makes it into the regions probed in these results due to radiation pressure accelerating Na antisunward.

radiation pressure, increasing the  $g$ -value relative to Mercury, so  $g_{\rho\odot}/g_M > 1$  and  $\tilde{N}/N > 1$ . On the dayside, the opposite happens: Ca ejected toward the Sun has a lower  $v_{\rho\odot}$  than Mercury, and therefore a smaller  $g$ -value and  $\tilde{N}/N < 1$ . Narrow regions exist over postdawn and predusk local times where Ca ejected toward the Sun is decelerated such that  $v_{\rho\odot} \sim v_{M\odot}$ . On the inbound portion of the orbit (TAA = 290°,

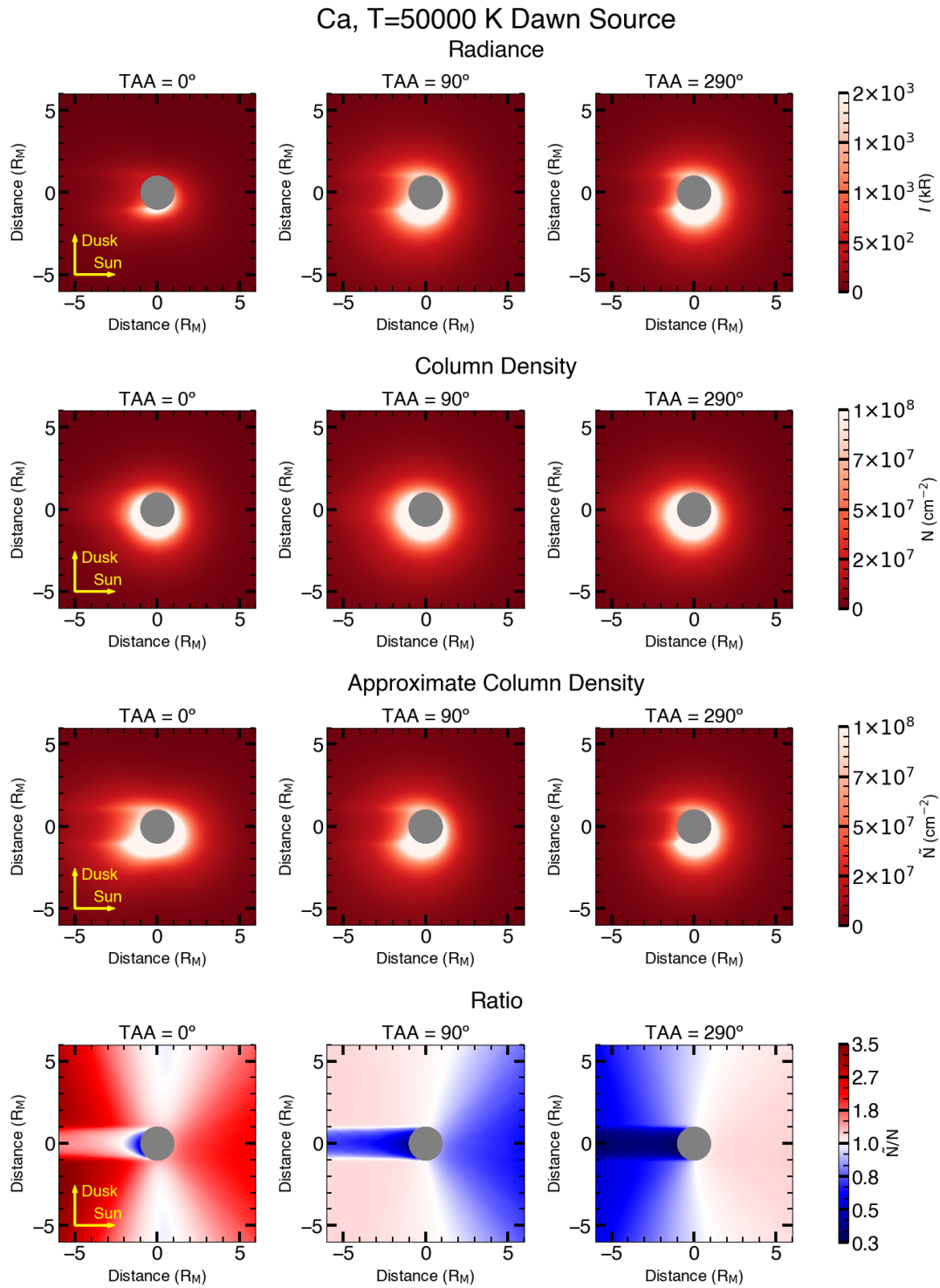


**Figure 10.** Same as Figure 9, using a 50,000 K, dawn-centered Ca source.

right columns), the opposite situation holds. The column density is underestimated on the nightside and, for Ca, overestimated on the dayside, again, because of the feedback loop.

#### 4. Discussion and Conclusions

Variations in the  $g$ -value affect both the radiance of the emitting (scattering) column density and the magnitude of the

radiation acceleration. Radiation acceleration acts in the antisunward direction to push atoms into a comet-like tail (W. H. Ip 1986; W. H. Smyth 1986). The effectiveness of sunlight to form this tail depends on the relative timescales for ballistic trajectories to return to the surface, for photoionization, and for antisunward transport by radiation acceleration. Ballistic timescales depend on the launch speed. The photoionization rate varies with species, but for a given species is assumed to vary only due to the  $r^{-2}$  dependence on

the solar flux (i.e., any dependence on solar activity has not been considered here). Radiation acceleration, as discussed above, is a function of both the distance from the Sun and the radial velocity of the atoms with respect to the Sun. Neither photoionization nor radiation acceleration operate in Mercury's geometric shadow.

We have detailed four effects of changing  $g$ -value that complicate the understanding of Mercury's exospheric sources and structure: (1) variations in the escape flux of atoms, (2) variations in the ratio of atoms that escape in neutral versus ionized form, (3) difficulties understanding exospheric source regions from the distributions of atoms in the exosphere, and (4) systematic uncertainties in determining emitting column densities of observed emissions without a priori knowledge of  $v_{\rho\odot}$  for each emitting atom.

MESSENGER UVVS observed seasonal variations in the Na tail (T. A. Cassidy et al. 2016, 2021), although that work did not determine whether the radiance variations were due to changing  $g$ -value or emitting column density. Our study demonstrates that both play a role: the escape rate of Na antisunward of Mercury is maximized when the  $g$ -value is maximized, so there are both more atoms scattering sunlight and more photons scattered per atom. Whether a tail always forms past  $\sim 4$ – $5$  Mercury radii ( $R_M$ ) from Mercury depends on the initial energy distribution of the Na. A PSD source at  $T \sim 1200$ – $1500$  K would likely only form a detectable tail at TAAs where  $v_{\rho\odot}$  is near its maximum. Hotter sources could produce a detectable tail at all TAAs, but would still show significant seasonal variability. Further analysis of the UVVS data, combined with models and observations of the deep Na tail  $> 1000 R_M$  from Mercury (J. Baumgardner et al. 2008; C. A. Schmidt et al. 2010), is needed to help better constrain the source of energetic Na from Mercury.

Our simulations show that for most Ca source scenarios—including monoenergetic and thermal distributions—radiation pressure has little impact on the escape flux. Even when Ca atoms reach escape speed, they are typically ionized close to the planet, limiting their contribution to the extended exosphere.

We also provide a demonstration of predictions of an annual asymmetry in the flux of escaping neutral atoms when Mercury is on the outbound portion of its orbit compared with the inbound portion (A. E. Potter et al. 2007; C. A. Schmidt et al. 2012). Atoms are more likely to escape when Mercury is moving away from the Sun than toward it. This is due to different feedback loops on the outbound and inbound portions induced because of variations in radiation pressure with heliocentric velocity. When an atom is moving away from the Sun, radiation acceleration increases its speed, which then increases the magnitude of the acceleration. When it is moving toward the Sun, radiation acceleration slows the atom down, which in turn decreases the radiation acceleration. Therefore, when Mercury is moving away from the Sun, (a) trajectories are more likely to be escaping than bound if photoionization is neglected, and (b) atoms on escaping trajectories escape faster, resulting in less photoionization. In summary, more escaping trajectories times more atoms along a trajectory reaching escape speed before being photoionized results in higher escape flux. This asymmetry is consistent with that seen in the UVVS Na tail observations (T. A. Cassidy et al. 2021), although pointing restrictions meant that UVVS could not observe the night side at perihelion and aphelion. It is therefore

not known whether the tail disappears at these TAAs or is just greatly diminished.

Model simulations of trajectories of atoms ejected from the surface under the influence of both gravity and radiation pressure show the difficulty of determining the source regions of the exosphere at the surface. Atoms ejected into the equatorial plane at  $\sim 2$ – $4 \text{ km s}^{-1}$  can be transported longitudinally around the planet, presenting a problem for interpreting observations. A MESSENGER UVVS spatial scan of the exosphere over the dusk hemisphere, for instance, would have been more sensitive to slow Na ejected from the near-dawn dayside than from the regions near dusk above  $\sim 1000$  km, with the ratio of dawn-to-dusk source Na increasing with altitude above the surface. If the source process ejects atoms with a wide range of speeds, it would be difficult or impossible to determine whether emission over the dusk limb was from Na ejected from the dawn or dusk hemisphere. Atoms that make it into the tail several Mercury radii antisunward could originate from almost anywhere on the surface. In a subsequent paper, we will discuss the detectability of Na in the tail by UVVS and implications for the exospheric Na source.

Finally, we have evaluated the common assumption that the column density of an emitting gas can be determined using a constant  $g$ -value. We find that the derivation of exospheric column density depends strongly on the  $g$ -values of the emitting atoms. Column densities derived using  $g$ -values assuming the emitting atoms are at rest relative to Mercury generally result in systematic errors in the determination of the emitting column density. Whether the derived column densities are over- or underestimated depends on the specific observing geometry, the epoch of the observations (i.e., TAA), and the initial source function. These errors can propagate into misinterpretations of surface density, source temperature derived from altitude profiles, and the nature of spatial asymmetries in exospheric sources.




The application of models of exospheric processes that can track the positions and velocities of exospheric neutrals greatly enhances the understanding of the source and loss processes in Mercury's exosphere. The MESSENGER UVVS observations of exospheric Na, Mg, and Ca have not been fully explored using such a model. Moreover, upcoming observations from the BepiColombo mission must similarly be interpreted using such a model, in particular those of the UV spectrograph Probing of Hermean Exosphere By Ultraviolet Spectroscopy (E. Chassefière et al. 2010) on the Mercury Planetary Orbiter and the Mercury Sodium Atmosphere Spectral Imager (I. Yoshikawa et al. 2010) on the Mercury Magnetospheric Orbiter.

### Acknowledgments

M.H.B., R.M.K., D.W.S., and O.J.T. were supported, in part, by NASA Solar System Workings Program Award No. 80NSSC22K0099. In addition, M.H.B., R.M.K., and R.J.V. were supported, in part, by NASA Discovery Data Analysis Program Award No. 80NSSC24K0063. L.M. was supported, in part, by the NSERC Discovery Grant and the CSA Research Opportunities in Space Sciences program awards.

*Software:* Astropy (Astropy Collaboration et al. 2013, 2018, 2022).

## ORCID iDs

Matthew H. Burger  <https://orcid.org/0000-0002-9334-7198>  
 Rosemary M. Killen  <https://orcid.org/0000-0002-0543-2326>  
 Ronald J. Vervack, Jr.  <https://orcid.org/0000-0002-8227-9564>  
 Orenthal J. Tucker  <https://orcid.org/0000-0002-8235-5440>  
 Liam S. Morrissey  <https://orcid.org/0000-0001-7860-9957>  
 Daniel W. Savin  <https://orcid.org/0000-0002-1111-6610>

## References

- Astropy Collaboration, Price-Whelan, A. M., Lim, P. L., et al. 2022, *ApJ*, **935**, 167
- Astropy Collaboration, Price-Whelan, A. M., Sipőcz, B. M., et al. 2018, *AJ*, **156**, 123
- Astropy Collaboration, Robitaille, T. P., Tollerud, E. J., et al. 2013, *A&A*, **558**, A33
- Baumgardner, J., Wilson, J., & Mendillo, M. 2008, *GeoRL*, **35**, L03201
- Berezhnoy, A. A. 2018, *Icar*, **300**, 210
- Berezhnoy, A. A., & Klumov, B. A. 2008, *Icar*, **195**, 511
- Bida, T. A., & Killen, R. M. 2017, *Icar*, **289**, 227
- Bida, T. A., Killen, R. M., & Morgan, T. H. 2000, *Natur*, **404**, 159
- Broadfoot, A. L., Shemansky, D. E., & Kumar, S. 1976, *GeoRL*, **3**, 577
- Burger, M. 2025, NEXOCLM: Neutral EXOsphere and CLoud Model, v3.6.1, Zenodo, doi:10.5281/zenodo.16897048
- Burger, M. H., Killen, R. M., McClintock, W. E., et al. 2012, *JGRE*, **117**, E00L11
- Burger, M. H., Killen, R. M., McClintock, W. E., et al. 2014, *Icar*, **238**, 51
- Burger, M. H., Killen, R. M., Vervack, R. J., et al. 2010, *Icar*, **209**, 63
- Cassidy, T. A., McClintock, W. E., Killen, R. M., et al. 2016, *GeoRL*, **43**, 11121
- Cassidy, T. A., Merkel, A. W., Burger, M. H., et al. 2015, *Icar*, **248**, 547
- Cassidy, T. A., Schmidt, C. A., Merkel, A. W., Jasinski, J. M., & Burger, M. H. 2021, *PSJ*, **2**, 175
- Chamberlain, J. W. 1961, *Physics of the Aurora and Airglow* (New York: Academic)
- Chamberlain, J. W., & Hunten, D. M. 1987, *Theory of Planetary Atmospheres* (New York: Academic)
- Chassefière, E., Maria, J. L., Goutail, J. P., et al. 2010, *P&SS*, **58**, 201
- Greene, T. P., Bell, T. J., Ducrot, E., et al. 2023, *Natur*, **618**, 39
- Huebner, W. F., & Mukherjee, J. 2015, *P&SS*, **106**, 11
- Ip, W. H. 1986, *GeoRL*, **13**, 423
- Killen, R., Shemansky, D., & Mouawad, N. 2009a, *ApJS*, **181**, 351
- Killen, R., Shemansky, D., & Mouawad, N. 2009b, *ApJS*, **182**, 667
- Killen, R. M., Burger, M. H., Vervack, R. J., & Cassidy, T. A. 2018, in *Mercury. The View after MESSENGER*, ed. S. C. Solomon, L. R. Nittler, & B. J. Anderson (Cambridge: Cambridge Univ. Press), 407
- Killen, R. M., Potter, A., Fitzsimmons, A., & Morgan, T. H. 1999, *P&SS*, **47**, 1449
- Killen, R. M., Vervack, R. J., Jr., & Burger, M. H. 2022, *ApJS*, **263**, 37
- Korth, H., Anderson, B. J., Johnson, C. L., et al. 2018, in *Mercury. The View after MESSENGER*, ed. S. C. Solomon, L. R. Nittler, & B. J. Anderson (Cambridge: Cambridge Univ. Press), 430
- Kreidberg, L., Koll, D. D. B., Morley, C., et al. 2019, *Natur*, **573**, 87
- Leblanc, F., Schmidt, C., Mangano, V., et al. 2022, *SSRv*, **218**, 2
- Lierle, P., Schmidt, C., Baumgardner, J., et al. 2022, *PSJ*, **3**, 87
- McClintock, W. E., Cassidy, T. A., Merkel, A. W., et al. 2018, in *Mercury. The View after MESSENGER*, ed. S. C. Solomon, L. R. Nittler, & B. J. Anderson (Cambridge: Cambridge Univ. Press), 371
- McClintock, W. E., & Lankton, M. R. 2007, *SSRv*, **131**, 481
- McClintock, W. E., Vervack, R. J., Bradley, E. T., et al. 2009, *Sci*, **324**, 610
- McCoy, T. J., Peplowski, P. N., McCubbin, F. M., & Weider, S. Z. 2018, in *Mercury. The View after MESSENGER*, ed. S. C. Solomon, L. R. Nittler, & B. J. Anderson (Cambridge: Cambridge Univ. Press), 176
- Meyer-Vernet, N. 2009, *Basics of the Solar Wind* (Cambridge: Cambridge Univ. Press)
- Milillo, A., Sarantos, M., Grava, C., et al. 2023, *SSRv*, **219**, 49
- Pokorný, P., Sarantos, M., & Janches, D. 2017, *ApJL*, **842**, L17
- Potter, A., & Morgan, T. 1985, *Sci*, **229**, 651
- Potter, A. E., Killen, R. M., & Morgan, T. H. 2007, *Icar*, **186**, 571
- Potter, A. E., & Morgan, T. H. 1986, *Icar*, **67**, 336
- Schmidt, C. A., Baumgardner, J., Mendillo, M., & Wilson, J. K. 2012, *JGRA*, **117**, A03301
- Schmidt, C. A., Wilson, J. K., Baumgardner, J., & Mendillo, M. 2010, *Icar*, **207**, 9
- Smyth, W. H. 1979, *ApJ*, **234**, 1148
- Smyth, W. H. 1986, *Natur*, **323**, 696
- Solomon, S. C., & Anderson, B. J. 2018, in *Mercury. The View after MESSENGER*, ed. S. C. Solomon, L. R. Nittler, & B. J. Anderson (Cambridge: Cambridge Univ. Press), 1
- Vervack, R. J., Killen, R. M., McClintock, W. E., et al. 2016, *GeoRL*, **43**, 11545
- Wurz, P., Fatemi, S., Galli, A., et al. 2022, *SSRv*, **218**, 10
- Yoshikawa, I., Korabev, O., Kameda, S., et al. 2010, *P&SS*, **58**, 224